

# Inelastic Relaxation Processes in Amorphous Sodium Silicates

Jessica M. Rimsza<sup>1</sup> and Reese Jones<sup>2</sup>

<sup>1</sup>Geochemistry Department, Sandia National Laboratories, Albuquerque, NM USA

<sup>2</sup> Mechanics of Materials, Sandia National Laboratories, Livermore, CA USA

## Abstract

During fracture amorphous oxides exhibit irreversible processes, including inelastic relaxation effects. Here, classical molecular dynamics simulations were used with a reactive forcefield to evaluate inelastic relaxation processes in five different amorphous sodium silicates. Overall, the 20% Na<sub>2</sub>O-SiO<sub>2</sub> composition exhibited the most inelastic relaxation during the simulation, followed by the 25% Na<sub>2</sub>O-SiO<sub>2</sub> composition, the 15% Na<sub>2</sub>O-SiO<sub>2</sub> composition, and finally the 10% and 30% Na<sub>2</sub>O-SiO<sub>2</sub> compositions. Coordination analysis of the Na<sup>+</sup> ions identified that during inelastic relaxation the Na<sup>+</sup> ions were increasingly coordinated by non-bridging oxygens (NBO), which was supported by radial analysis of the O-Na-O bond angles surrounding the crack tip. Across the sodium silicate compositional range, two different inelastic relaxation mechanisms were identified based on the amount of bridging oxygens (BO) and NBOs in the Na<sup>+</sup> ion coordination shell. Two different inelastic relaxation mechanisms were identified based on the amount of bridging oxygen (BO) and NBO in the Na<sup>+</sup> ion coordination shell. In the lower Na concentration systems where the Na<sup>+</sup> ions were primarily coordinated by BO, inelastic relaxation was enabled by Na<sup>+</sup> ion migration toward the crack tip. In contrast, a change in the inelastic relaxation mechanism occurred when the Na<sup>+</sup> ions were coordinated by primarily NBO in the higher concentration systems. In this case the entire structure relaxed toward the crack tip rather than isolated migration of the Na<sup>+</sup> ions. By developing a fundamental understanding of how modified silica systems respond to static stress fields, we will be able to predict slow crack growth.

## I. Introduction

Creating durable amorphous oxides is a perennial challenge in the development of reliable material systems, including optics and microelectronics.<sup>1, 2</sup> Fracture of amorphous oxides occurs in three distinct regimes which vary with the stress intensity.<sup>3</sup> Region III occurs at loading rates higher than the stress intensity factor ( $K_{IC}$ ) and crack velocities approach the terminal values.

Region II is attributed to a diffusion-controlled region that is independent of applied stress in a reactive environment.<sup>4</sup> Region I occurs at the lowest stress intensities, and has been attributed to chemical effects, for example from water interacting with strained bonds at the crack tip.<sup>5, 6</sup> The slow crack growth rates identified in Region I are of particular interest because they can cause failure of seemingly stable systems after weeks, months, or years of microscopic crack growth until a critical flaw length is reached and the crack growth accelerates into one of the other fracture regimes.

Understanding the mechanisms that cause crack growth in Region I are complicated by competing factors in the amorphous structure. Generally, oxides are considered brittle materials. Brittle fracture has been described by linear elastic fracture mechanics (LEFM) for the last century<sup>7</sup>, based on the mechanism that crack growth occurs when the energy near the crack tip is greater than that of the addition of new surface area.<sup>8</sup> Yet, it has been established that amorphous oxides have a local region surrounding the crack tip that exhibits inelastic effects, which allow for stress dissipation via mechanisms that do not add surface area.<sup>9</sup> Additionally, a strong dependence of crack growth on the presence of even small amounts of humidity indicates that the environment can facilitate bond breakage and is a significant factor in crack propagation at low strain.<sup>10-12</sup> Nevertheless slow crack growth does occur even under vacuum conditions<sup>13, 14</sup>, suggesting that the formation of surface area and inelastic relaxation are integral to crack propagation.

The competing mechanisms of surface area formation and inelastic relaxation have been incorporated into numerous fracture models, including a recent transition-rate-theory model for identifying the stress-intensity threshold, which is a stress-intensity below which a crack will not propagate.<sup>15</sup> The model assumes that termination of crack velocity is due to inelastic stress relaxation in the region surrounding the crack tip, in addition to surface energy, and was used to predict stress intensity thresholds for soda-lime-silicate compositions.<sup>15</sup>

The development of this stress-intensity threshold model<sup>15</sup> as well as other transition-rate-theory models<sup>16-18</sup> has highlighted the role of how inelastic relaxation mechanisms control slow-crack growth. Inelastic relaxation effects in the region surrounding the crack tip in amorphous oxides are particularly challenging to characterize due to the small size of the process zone, which is estimated to be only a few nanometers across.<sup>6, 19</sup> Additionally, defects can be difficult to quantify in amorphous oxides using common characterization methods in comparison to crystalline systems with well-organized microstructures. The challenges are even more acute

when comparing the same composition under different stress states or over temporal scales. In this case molecular models such as classical molecular dynamic (MD) simulations are uniquely well suited to evaluate how the structure of the amorphous oxide changes in a stress field. Not only can classical MD be applied to systems the size of the inelastic zone, but the amorphous atomic configurations can be extensively analyzed to quantify small changes in the structure.

Previously, classical MD simulations have been used to evaluate mechanical properties<sup>20-25</sup>, tensile fracture<sup>26-28</sup>, and the effect of chemical effects on fracture<sup>23, 29, 30</sup> across a variety of compositions. Additionally, inelastic relaxation effects have been evaluated for amorphous silica, identifying that defect concentrations varied around the crack tip during relaxation, including the formation of a high defect concentration ahead of the crack tip.<sup>31</sup> Critically, most glasses used in practical applications include some network modifiers. These modifiers, including Na<sup>+</sup>, break-up the networked oxide structure and as coordinated, but not bonded species, have different dynamics and coordination structures than the network formers. Here, we have used a recently published Na/Si/O reactive forcefield<sup>32</sup> to evaluate how five different amorphous sodium silicates over a range of compositions relax under static far-field loading conditions, building on previous studies of inelastic relaxation in silica and dynamic loading effects on silica and sodium silicates.<sup>33</sup> Change in the system energy is related to structural rearrangement of the system to identify how the applied stress is accommodated by the amorphous oxide structure, including Na<sup>+</sup> ion coordination and migration through the system.

## II. Computational Methods

The classical MD simulations in this study were performed using a reactive classical MD force field (ReaxFF)<sup>34,35</sup>, which was parametrized for amorphous sodium silicates.<sup>32</sup> ReaxFF allows for bond breakage and formation through recalibration of partial atomic charges, and has been extensively used for evaluation of fracture.<sup>19, 29, 30, 36-39</sup> Quasi-2D simulation cells (150 Å x 150 Å x 25 Å) of sodium silicates were created through a melt-and-quench procedure. Deng et al.<sup>40</sup> performed an exhaustive evaluation of protocols for generating sodium silicates using several different forcefields, including Teeter<sup>41</sup>, a ReaxFF version parameterized by Yu et al.<sup>42</sup>, and the Na/Si/O ReaxFF forcefield used here.<sup>32</sup> Based on these results, we used the Pedone forcefield<sup>43</sup> for the initial melt and quench protocol, which has previously been used to simulate a variety of

modified oxide structures with experimentally validated structural and mechanical properties, followed by an annealing step with ReaxFF.

**Table 1:** System size and composition of amorphous sodium silicates.

	Composition (atoms)		
	Na	Si	O
<b>NS10</b>	2550	11525	24325
<b>NS15</b>	3850	10875	23675
<b>NS20</b>	5100	10250	23050
<b>NS25</b>	6400	9600	22400
<b>NS30</b>	7700	8950	21750

Five different amorphous sodium silicates were generated, from 10 mole % Na<sub>2</sub>O (NS10) to 30 mole % Na<sub>2</sub>O (NS30) in 5 mole % increments. Initially a simulation box with the mixture of Na, Si, and O atoms necessary for the composition of interest (see Table 1) was generated with random atomic positions. These randomized structures underwent a melt and quench protocol: first heating the system to 3500 K at a rate of 100 K/picosecond (ps), holding the simulation at 3500 K for 100 ps, and then cooling to 300 K at a rate of 5 K/ps with a 0.5ps time step. The final cooled structure then underwent a 100 ps equilibration at 300 K. All steps used an isothermal-isobaric ensemble (NPT) with a 1.0 femtosecond (fs) time step damping parameter equal to 100 time steps for the thermostat and 1000 time steps for the barostat. Following this melt, quench, and equilibration procedure with the Pedone forcefield, an annealing step with the Na/Si/O ReaxFF forcefield was performed. The sodium silicate structures were heated from 300 K to 1500 K at a rate of 5 K/ps, held at 1500 K for 80 ps, and cooled at a rate of 5 K/ps back to 300 K using a 0.25 fs time step. The annealing procedure also used a NPT ensemble, with a damping parameter equal to 100 time steps for the thermostat and 1000 time steps for the barostat. A final equilibration was performed in a canonical (NVT) ensemble for 10 ps with a 0.25 fs time step. The final sodium silicate structures were used for evaluation of the inelastic relaxation properties in highly strained stress fields. Data on the structural features of the resulting bulk sodium silicates have been reported in previous publications.<sup>33</sup> All simulations were performed using the LAMMPS MD code with the USER-REAXC package.<sup>44</sup>

For evaluation of inelastic relaxation, a perfect slit crack was created in the sodium silicate structures by removing interactions between upper and lower sets of atoms separated by a plane extending halfway into the system (see Figure 1). To sample the anisotropy expected in the

amorphous systems, the original sodium silica structure was rotated by 90° three times and a slit crack was introduced into the same half plane to create four distinct systems. The average and standard error of the four simulations are reported throughout the manuscript unless otherwise noted.

The crack was mechanically loaded by displacement of far-field atoms in a region outside a cylinder centered on the crack tip. The active region has a radius of 6.5 nm. Previous studies based on gold (fcc), iron (bcc), and silica calculated a J-integral for varying system sizes, which indicated that the process zone was contained within 5-8 nm of the crack tip.<sup>45</sup> The far-field atoms are displaced and then fixed to maintain the loading over the course of the simulation. The displacement field ( $u_1, u_2$ ) was taken from the LEFM continuum solution for a semi-infinite slit crack in mode I loading<sup>46</sup> in Equation 1.a and 1.b:

$$u_1 = \frac{K_I}{2G\sqrt{2\pi}} \cos\left(\frac{\theta}{2}\right) \left[ k - 1 + 2\sin^2\left(\frac{\theta}{2}\right) \right] \quad (1.a)$$

$$u_2 = \frac{K_I}{2G\sqrt{2\pi}} \sin\left(\frac{\theta}{2}\right) \left[ k + 1 - 2\cos^2\left(\frac{\theta}{2}\right) \right] \quad (1.b)$$

The displacement field is spatially varying ( $r, \theta$  are polar coordinates) and is parameterized by the stress intensity factor  $K_I$ . The result is a prescribed displacement for each far-field atom that is a function of the atom's distance from the crack tip. Under this loading, the slit crack develops a stress singularity that is characteristic of all classical cracks prior to relaxation,<sup>47</sup> which is distinct from notch geometries.<sup>48, 49</sup> The shear modulus ( $G$ ) and the Poisson's ratio ( $\nu$ ) that were used to construct the far-field plane strain mode I loading are based on previous calculations of the mechanical properties of sodium silicates produced with the same computational procedure.<sup>33</sup> The crack was opened in one step to a  $K_I$  value of  $2 \times 10^{-2} \text{ MPa}\sqrt{\text{m}}$  via the prescribed displacement field and then underwent 1000 ps (1 nanosecond) of relaxation at a temperature of 0.1 K. There are methods of using temperature assisted dynamics to access these longer times<sup>31</sup>, but in this study we have elected to focus on the fast relaxation that occurs when the crack tip has just been formed.

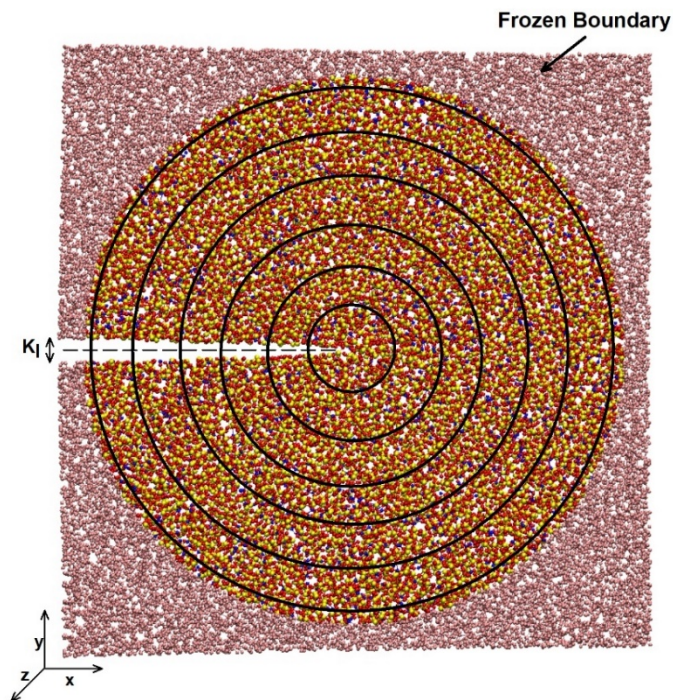


**Figure 1:** Schematic of far-field loading conditions. The pink atoms are the frozen boundary with prescribed displacement via Equation 1. Concentric circles outline radial shells used for analysis. Atom colors in the active region: oxygen (red), silicon (yellow), sodium (blue)

### III. Results

#### i. Crack Growth

Overall, during the relaxation of the loaded amorphous sodium silicates, crack growth of less than 5 Å occurred. This low amount of crack growth was expected, since the short temporal and spatial features of MD simulations can make it challenging to model the rare events that factor into crack growth at longer time scales. Observed crack growth was between 0-4 Å over the 1000 ps of relaxation time. The most crack growth occurred in the NS20 system with an average crack growth of  $1.02 \pm 1.72$  Å, followed by NS15 ( $0.30 \pm 0.52$  Å), NS10 ( $0.28 \pm 0.14$  Å), NS30 ( $0.23 \pm 0.11$  Å), and NS25 ( $0.00 \pm 0.00$  Å). Calculated crack length was defined based on the atom density of the quasi-2D system calculated on a rectangular grid with spacing 1 Å spacing in in x and y. The vacuum-sodium silicate edge was identified with where the atom density goes from zero to greater than zero. The crack surface of sodium silicate structure is fit to a parabola, and the crack depth is defined as the change in the location of the vertex from the initial step to the selected loading step. This method identifies overall changes in the length of the empty space that defines the interior of

the crack, rather than using other recently reported methods based on the observed displacements and the stress intensity factor.<sup>50</sup>

## **ii. Inelastic Relaxation**

All crack growth occurred in the first ~150 ps of the simulation, as seen in Figure 2. The early crack growth occurs is indicative of stress-relaxation processes as seen in amorphous silica<sup>31</sup>, where rearrangement of the amorphous structure, including the breaking and formation of bonds, is necessary to relax the stress in the system. The evolution of the stress is related to internal energy which includes strain energy. Total change in potential energy is included in Figure S1. Analyzing the change in potential energy limits the impact of the thermostat on the results and focuses on the changes in the structure. The change in the potential energy indicates that all the sodium silicate compositions exhibited exponential decay in the potential energy during inelastic relaxation with  $R^2$  values between 0.87-0.99. It is notable that the inelastic relaxation occurred even at the near-zero temperatures studied here, since previous work on inelastic relaxation in amorphous silica found that measurable relaxation only occurred at temperatures of 300 K or greater.<sup>31</sup> The exponential decay fits of the change in potential energy versus inelastic relaxation time are plotted in Figure 3. It is evident from the decay that the relaxation occurred within the duration of the simulation; minimal additional relaxation is expected if the simulation time were to be extended. Significantly, there is a compositional dependence on the total amount of relaxation. The highest change in potential energy during inelastic relaxation occurs in the NS20 composition, followed by NS25, NS15, and then NS10~NS30. These results suggest that there is a structural feature in the NS20 composition that allows for this faster relaxation.

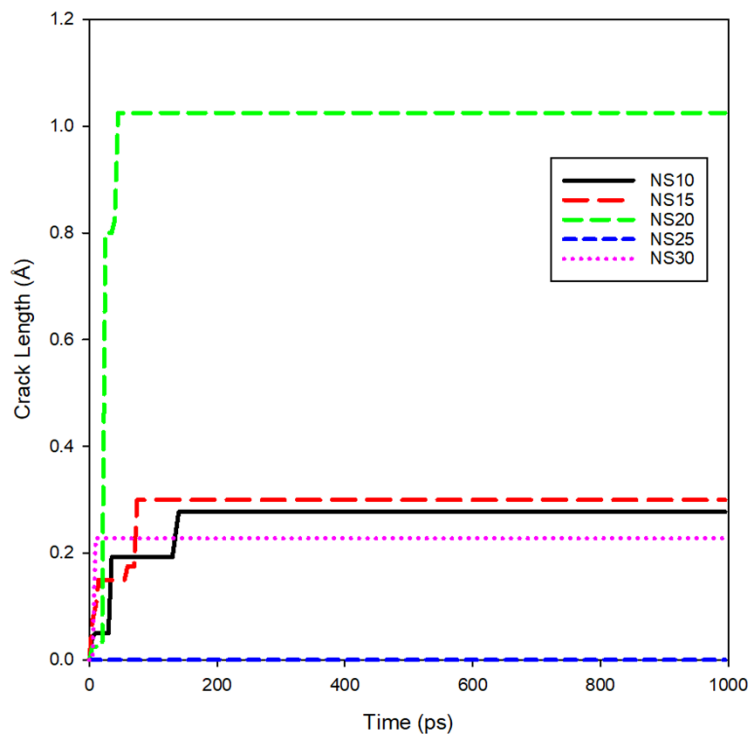


**Figure 2:** Fracture length versus relaxation time for sodium silicate systems. Error bars removed for clarity.

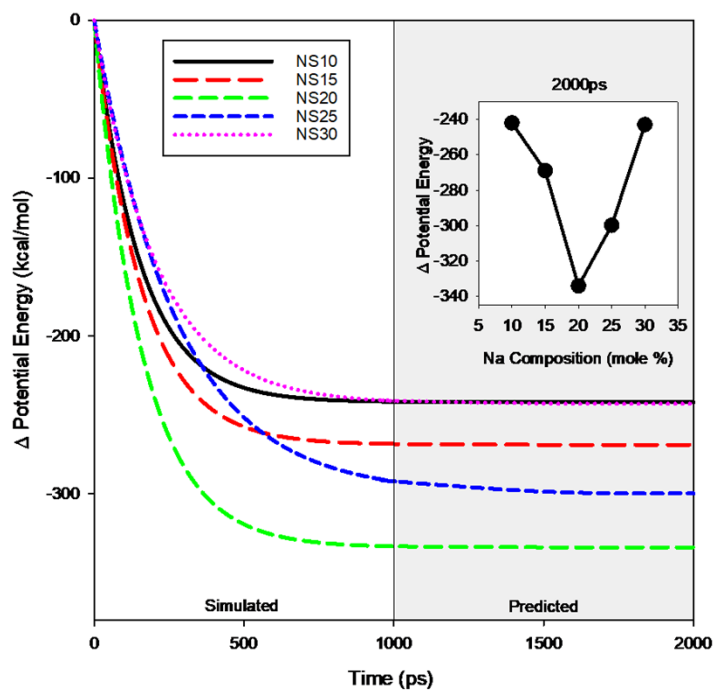


**Figure 3:** Change in potential energy versus time for loaded cracks in sodium silicates from an exponential decay fit of the four different simulations per composition. The shaded region

indicates a prediction for further decreases in potential energy. Inset includes the change in potential energy versus composition from the exponential decay fit at 2000ps.

The change in the total potential energy is correlated with the amount of fracture that occurred in the system, as seen in Figure 4. The sodium silicate composition with the highest change in potential energy (NS20) had the most crack growth, compared with simulations with the lowest changes in potential energy (NS10 and NS30). The addition of new surface area via fracturing cannot account for all the change in potential energy since (i) additional surface area with no inelastic relaxation would *raise* the potential energy of the system due to the addition of new broken bonds and (ii) the potential energy of the system continues to decrease even when all the fracturing has completed. For example, in the case of NS20 all the fracture events have occurred within the first 50ps of the simulation, but nearly 70% of the potential energy decrease occurs later in the simulation. Therefore, the amount of inelastic relaxation that a sodium silicate exhibits cannot be entirely accounted for by the formation of new surface area, indicating the presence of additional inelastic effects.

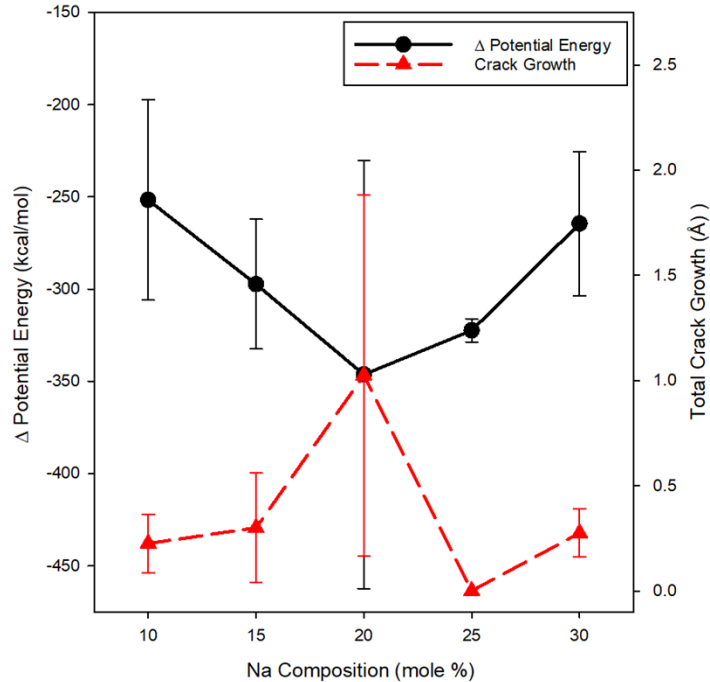


**Figure 4:** Total change in potential energy and crack growth versus sodium concentration in amorphous sodium silicate.

### iii. Structural Relaxation

The decrease in potential energy is associated with changes in the structure of the sodium silicate, through either the formation of surface area via breaking of atomic bonds, as previously discussed, or in surface stretching and deformation of the structure without crack growth. Previous investigations of dynamic loading of sodium silicates also found limited changes in the silica structure of the system<sup>33</sup>, and the effects on inelastic relaxation are expected to be even more limited during the static loading conditions used here. The similarity of the global structural descriptors (bond lengths, bond angles) following inelastic relaxation indicates that there is not a loss of the amorphous structure or significant formation of defects or cavities from relaxation processes that have been seen in other studies.<sup>51</sup>

There is a strong *radial* dependence on the amount of structural rearrangement during inelastic relaxation. Here, we separated out the portion of the structure closest to the crack tip through a cylindrical cut-out with a radius of 10 Å. Atoms farther from the crack tip are binned via concentric cylinders centered at the crack tip that increase in size. See a schematic in Figure 1. Figure 5 includes the change in the average O-Na-O bond angle for the NS20 condition, which exhibited the most inelastic relaxation. During inelastic relaxation the average O-Na-O bond angle decreases from  $103.6 \pm 3.2^\circ$  to  $101.8 \pm 1.4^\circ$ . In addition to the overall decrease in the average bond angle, the amount of error decreases as well, indicating that the relaxation is removing O-Na-O bond angles that are outliers and lowering the variability in the O-Na-O angles towards a more consistent value.

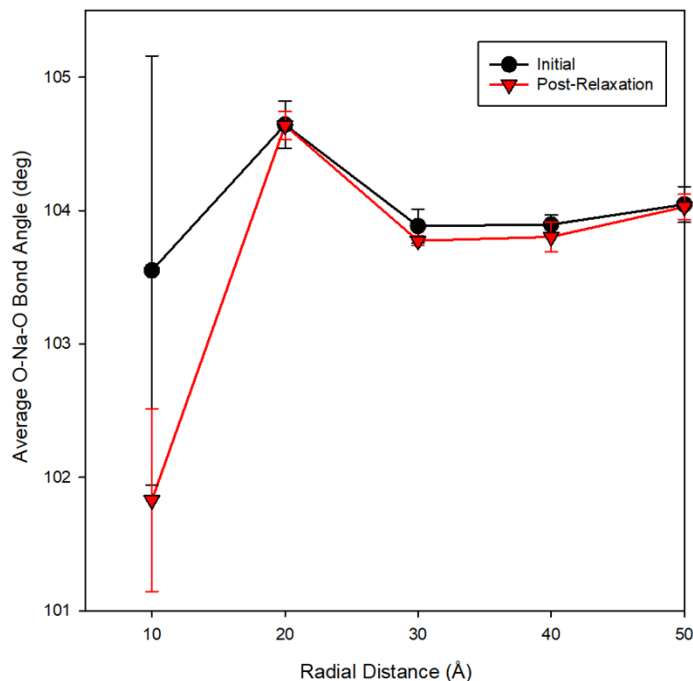


**Figure 5:** Change in average O-Na-O angle in the NS20 composition as a function of radial distance, pre (black) and post (red) relaxation.

The Na $\cdots$ O coordination environment can also identify how the Na $^+$  ions are interacting with the network structure. The Na $\cdots$ O coordination environment was identified using a Na $\cdots$ O cut-off distance of 3.0 Å and a Si-O cut-off distance of 2.25 Å with an average Na $\cdots$ O coordination of  $\sim 4.5$ , consistent with previous reports of sodium silicates.<sup>52</sup> Also, from the initial to the final state the change in Na $\cdots$ O coordination is negligible, from  $4.46 \pm 0.03$  to  $4.46 \pm 0.04$  across all replicates and compositions. The change in the type of coordinating oxygen, either bridging oxygen (BO), which is a oxygen bound to two silicon, or a non-bridging oxygen (NBO) which is a oxygen bound to one silicon, is more distinct. As seen in Figure 6 the total change in coordination for each composition within the first 10 Å of the crack tip is limited. Decreases in Na $\cdots$ BO coordination is balanced by increases in Na $\cdots$ NBO concentration. Also, there is a clear distinction at NS20, where the change in the Na $\cdots$ BO and Na $\cdots$ NBO coordination are nearly zero. At higher and lower sodium concentrations there is a clear increase in Na $\cdots$ NBO coordination at the expense of Na $\cdots$ BO. Additionally, between the NS15 and NS20 composition is when Na $\cdots$ NBO coordination becomes the dominate species (Figure 7), and the NS20 composition is when the Na-NBO/Na-BO concentration are most equal. This transition from Na $^+$  ions primarily coordinated by BO to being

coordinated by NBO has been noted in bulk sodium silicate structures<sup>52</sup>. The transition in Na<sup>+</sup> ion coordination, from primarily BO to NBO, suggests that there may be a mechanistic difference in how the amorphous oxide structure is relaxing based on the connectivity of the network and the mobility of the Na<sup>+</sup> ions.

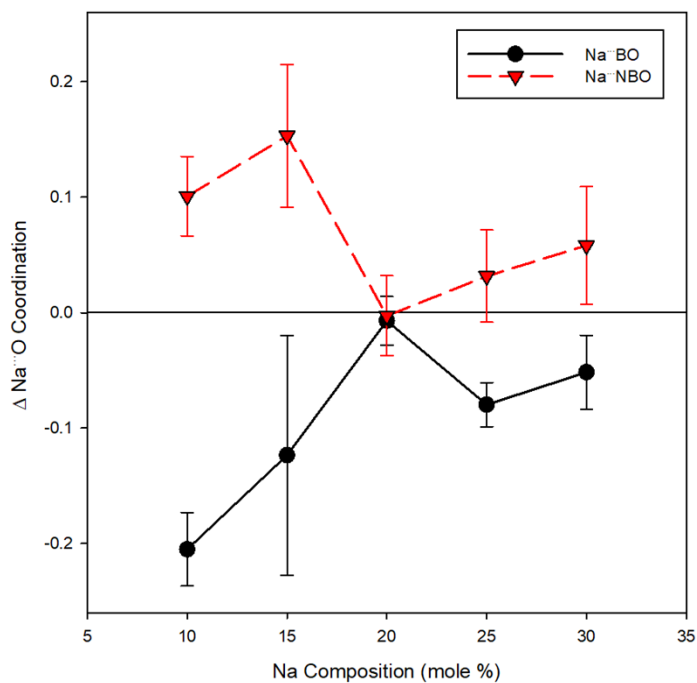


**Figure 6:** Change in Na···O coordination shell by oxygen type (bridging oxygen = BO, non-bridging oxygen = NBO) within the first 10Å of the crack tip.

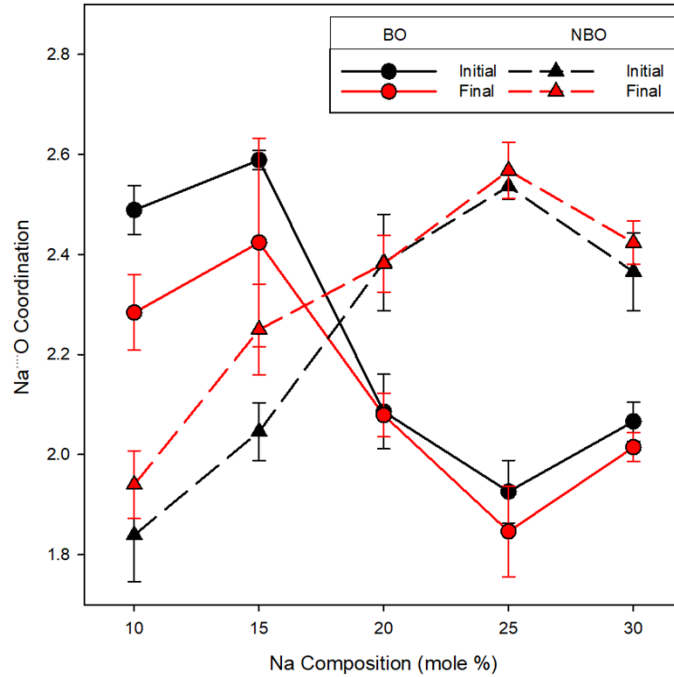


**Figure 7:** Speciation in Na-O coordination shells as a function of sodium silicate composition.

#### iv. Ion Migration During Inelastic Relaxation

The lack of explicit Na-O bonds in the system indicates that the  $\text{Na}^+$  ion is more mobile than Si and O atoms in the system, specifically in the presence of an applied external stress field. Therefore, we look at the initial and final location of all the atoms in the system, relative to the location of the crack tip. By calculating the radial component of the displacement vector for each atom, the directionality of the atomic migration can be analyzed. The per-atom migration was based on its position at the first and last frame of the simulation. Then atoms were separated by element and binned in  $1 \text{ \AA} \times 1 \text{ \AA}$  2-dimensional bins and the displacements averaged. The results are included in Figure 8. Blue indicates that the atom is moving *toward* the crack tip, while the red indicates its moving *away* from the crack tip. Here, the region ahead of the crack tip has the least amount of atomic migration, despite the comparable displacement fields (Figure S2). It should also be noted that a divergence for the  $\text{Na}^+$  ion migration pattern occurs near the crack tip, where the most atomic migration occurred (indicated by the darker colors) and along the surface, where the atoms are moving away from the crack tip. In the latter case, this arises from relaxation of the surface. It has been established in multiple MD studies that the free surface causes significant ion migration, including in modified glasses such as sodium silicates<sup>53, 54</sup>, and similar phenomena are

expected to occur here. There is an even more narrowly defined region, less than 10 Å from the crack tip, which exhibits the most atomic migration. Quantification of this effect is discussed in the next section.

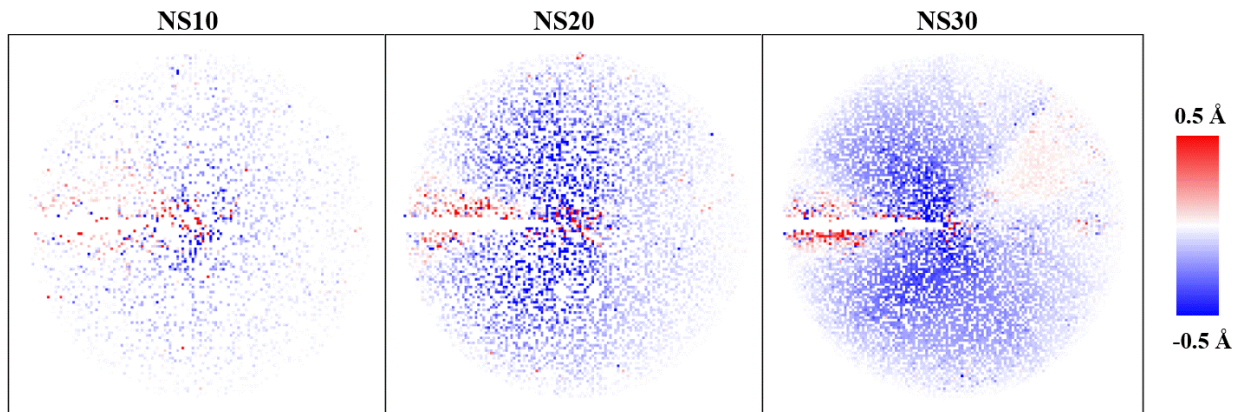


**Figure 8:** Average and binned radial per-atom  $\text{Na}^+$  ion migration in NS10, NS20, and NS30 compositions.

#### v. Atomic Migration

Maps of the average atomic migration in the process zone, discussed in the previous section, have highlighted that there is a qualitative change in the amount of atomic migration as a function of the sodium silicate composition. Therefore, quantification of atomic migration as a function of radial distance was performed to identify how atomic migration is connected to inelastic relaxation. Figure 9 includes the average atomic migration of  $\text{Na}^+$  ions in the system, binned by their distance from the crack tip. The global trend demonstrates that farther from the crack tip, the  $\text{Na}^+$  ions move smaller distances which is consistent with the displacement field (Figure S2). At radial distances less than 30 Å, the trend diverges, with NS20 exhibiting the most atomic migration away from the crack tip.

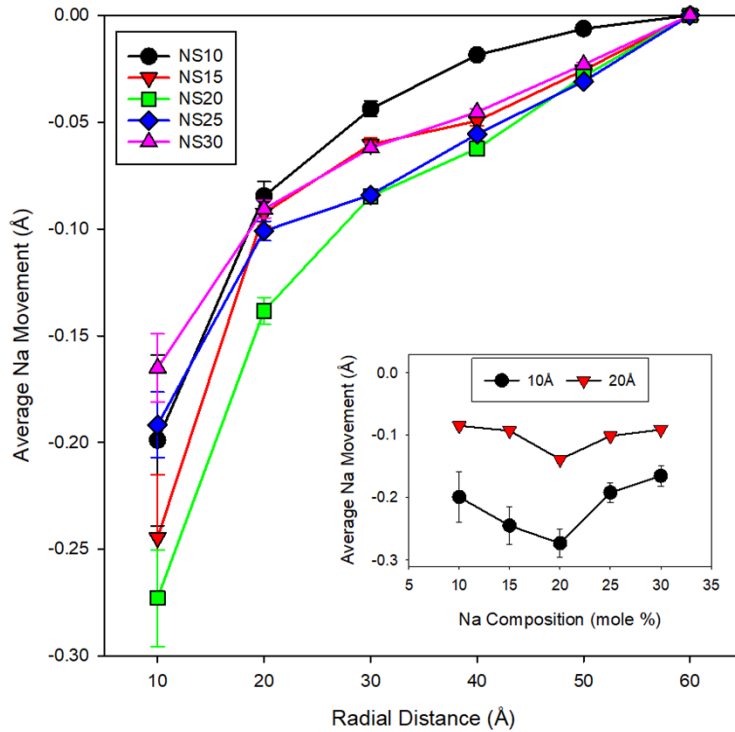


**Figure 9:** Change in average radial  $\text{Na}^+$  ion migration as a function of radial distance for sodium silicates. Inset change in average  $\text{Na}^+$  ion movement for radial distance of 10 Å and 20 Å

Separating out the atomic types can provide more insight into this phenomenon. As seen in Figure 10, the  $\text{Na}^+$  ions exhibit the most atomic migration across the compositions. This is followed by the NBO species, and for the NS15 compositions the amount of Na and NBO migration is nearly equivalent. In comparison, BO and Si migration is significantly lower and trend together, consistent with their strongly networked structure. For NS20 and sodium silicate compositions with higher sodium concentrations there is a clear decrease in the amount of atomic migration. Conversely for sodium silicate structures with compositions lower than NS20, the Na and NBO migration behaves more inconsistently, with the amount of migration balanced between the two atomic species.

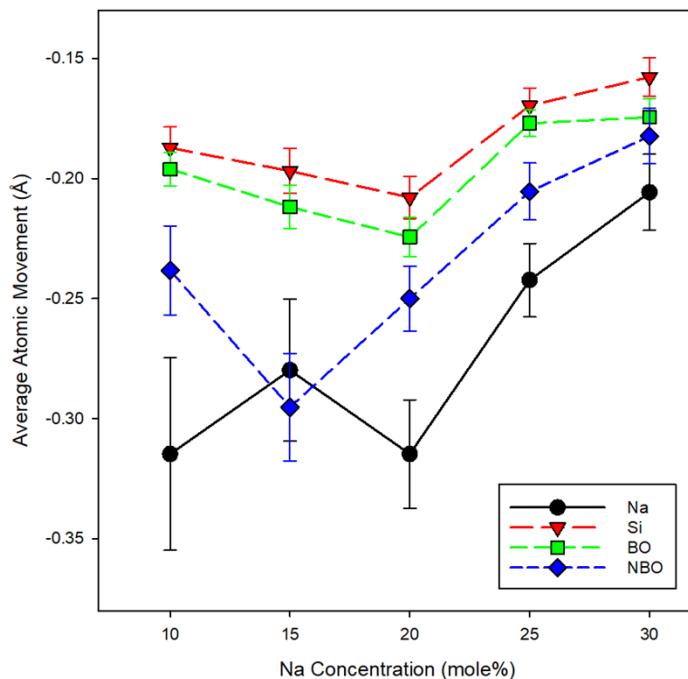


**Figure 10:** Average radial atomic migration within the first 10 Å of the crack tip, separated by atomic species.

Analysis of the inelastic relaxation in these sodium silicate systems has consistently demonstrated variation with composition in the response to static loading, with NS20 acting as a pivot point between two different mechanisms. This same variation was noted in analysis of dynamic loading of sodium silicates, suggesting that high sodium concentrations resulted in greater structural changes during dynamic fracture.<sup>33</sup>

Based on our current and previous data, we hypothesize the existence of two distinct mechanisms, based on if  $\text{Na}^+$  ion is coordinated by primarily BO versus NBO. At lower sodium concentrations, when the  $\text{Na}^+$  ions are coordinated by primarily BO, the network structure is more intact and the  $\text{Na}^+$  ions are more mobile. Cormack and Zeitler noted that in amorphous sodium silicates with low sodium concentrations, the lack of  $\text{NBO} \cdots \text{Na}^+$  interaction allow the  $\text{Na}^+$  ion to more easily diffuse through the structure until it becomes coordinated by a NBO.<sup>55</sup> As a result,  $\text{Na}^+$  ions can more easily diffuse toward the crack tip in the applied stress field, which accounts for the majority of the inelastic relaxation. In contrast at higher  $\text{Na}^+$  concentration, when the  $\text{Na}^+$  ions are primarily coordinated by NBO, the  $\text{Na}^+$  ions are more stable in their binding configurations and the silica network is more fragile. As a result, the atomic species move together, and it is the

contraction of the entire amorphous silica network toward the crack tip that is the driving force for inelastic relaxation.

To test this hypothesis, the average atomic migration for the  $\text{Na}^+$  and Si species was plotted against the change in the potential energy (see Figure 11). Note that due to the variation in the energy dissipation between replicates, each replicate was plotted separately. Figure 11.a. includes the data for the NS10 and NS15 compositions. The average  $\text{Na}^+$  ion migration is highly correlated with the change in the potential energy ( $R^2 = 0.71$ ) with more negative  $\text{Na}^+$  ion migration associated with less inelastic relaxation. Additionally, in a few cases the  $\text{Na}^+$  ion migration is positive and is associated with the most inelastic relaxation. In contrast, the average Si migration shows only a loose correlation with dissipation energy ( $R^2 = 0.43$ ). Therefore, it is plausible that the  $\text{Na}^+$  ions are migrating independently of the silica network. These trends are distinctly different in the high sodium compositions, NS20, NS25, and NS30. As seen in Figure 11.b. the amount of  $\text{Na}^+$  ion and Si migration are very similar and highly correlated with inelastic relaxation ( $R^2 = 0.77$ ) The distinct differences in how the atomic species relax in the far-field loading conditions supports the existence of these two different atomic mechanisms for inelastic relaxation depending on the diffusivity of the network modifier.

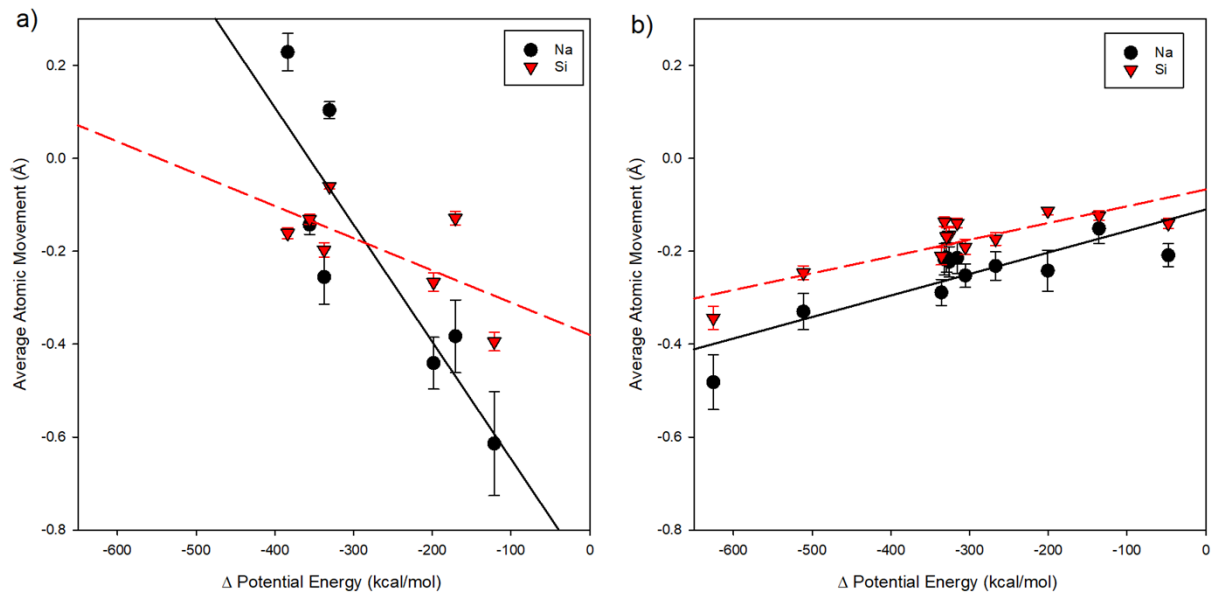


**Figure 11:** Average atomic movement for  $\text{Na}^+$  ions and Si versus the change in potential energy for (a) NS10 and NS15 compositions and (b) the NS20, NS25, and NS30 compositions. Solid and dotted lines are linear fits.

#### **IV. Conclusion and Summary**

Amorphous oxides exhibit irreversible processes during fracture, including the presence of inelastic effects. To understanding this process, classical MD simulations of structural relaxation surrounding a crack tip were performed for five different amorphous sodium silicate compositions using a reactive forcefield. The most inelastic structural relaxation occurred in the 20% Na<sub>2</sub>O-SiO<sub>2</sub> system, followed by the 25% Na<sub>2</sub>O system, the 20% Na<sub>2</sub>O system, and then the 10/30% Na<sub>2</sub>O systems. The amount of inelastic relaxation was correlated with the amount of crack growth that occurred but was unable to capture all inelastic relaxation affects. Globally, the changes in the amorphous structure during relaxation were minimal; however, within the first 10 Å of the crack tip a decrease in the O-Na-O bond angle occurred, indicative of the formation of more BO-Na-BO bonds from relaxation. Further changes occurred in the coordination shell of the Na<sup>+</sup> ion, including the tendency for greater coordination by NBO following inelastic relaxation. The effect of the Na<sup>+</sup> coordination shell on inelastic relaxation were separated out by systems with Na<sup>+</sup> ions primarily coordinated by BO (NS10, NS15) and those with higher sodium concentrations and Na<sup>+</sup> ions primarily coordinated by NBO (NS20, NS25, NS30). For low sodium concentrations, the Na<sup>+</sup> ion migration is highly correlated with the amount of inelastic relaxation, in comparison to the Si atoms which exhibit less migration and little relation to the migration of the Na<sup>+</sup> ion. In contrast, for systems with higher sodium concentrations, the migration of the Na<sup>+</sup> ion and Si are extremely similar, and both are highly correlated to inelastic relaxation ( $R^2 = 0.78$ ). This indicates that two different inelastic relaxation mechanisms are occurring in the system. At low sodium silicate compositions, the sodium, as the mobile species, is migrating toward the crack tip while the network structure remains in place. In contrast at higher sodium concentration, relaxation of the entire system is occurring, due to increased flexibility in the network structure from the high concentration of Na<sup>+</sup> ions. By developing a fundamental understanding of how modified silica systems respond to static stress fields, we will be able to predict slow crack growth.

#### **V. Acknowledgement and Support**

This article has been authored by an employee of National Technology & Engineering Solutions of Sandia, LLC under Contract No. DE-NA0003525 with the U.S. Department of Energy (DOE). The employee owns all right, title and interest in and to the article and is solely responsible for its contents. The United States Government retains and the publisher, by accepting the article for

publication, acknowledges that the United States Government retains a non-exclusive, paid-up, irrevocable, world-wide license to publish or reproduce the published form of this article or allow others to do so, for United States Government purposes. The DOE will provide public access to these results of federally sponsored research in accordance with the DOE Public Access Plan <https://www.energy.gov/downloads/doe-public-access-plan>.

## References:

1. Bude, J.; Miller, P.; Shen, N.; Suratwala, T.; Laurence, T.; Steele, W.; Baxamusa, S.; Wong, L.; Carr, W.; Cross, D. In *Silica laser damage mechanisms, precursors, and their mitigation*, Laser-Induced Damage in Optical Materials: 2014, SPIE: 2014; pp 108-120.
2. Vella, J.; Adhihetty, I.; Junker, K.; Volinsky, A., Mechanical properties and fracture toughness of organo-silicate glass (OSG) low-k dielectric thin films for microelectronic applications. *Int. J. Fract.* **2003**, *120*, 487-499.
3. Varshneya, A. K., *Fundamentals of inorganic glasses*. Elsevier: 2013.
4. Quackenbush, C.; Frechette, V., Crack-front curvature and glass slow fracture. *J. Amer. Ceram. Soc.* **1978**, *61* (9-10), 402-406.
5. Freiman, S. W.; Wiederhorn, S. M.; Mecholsky, J., John J, Environmentally enhanced fracture of glass: a historical perspective. *J. Amer. Ceram. Soc.* **2009**, *92* (7), 1371-1382.
6. Ciccotti, M., Stress-corrosion mechanisms in silicate glasses. *J. Phys. D: Appl. Phys.* **2009**, *42* (21), 214006.
7. Orowan, E., The fatigue of glass under stress. *Nature* **1944**, *154* (3906), 341-343.
8. Griffith, A. A., VI. The phenomena of rupture and flow in solids. *Philosophical transactions of the royal society of london. Series A, containing papers of a mathematical or physical character* **1921**, *221* (582-593), 163-198.
9. Célarié, F.; Ciccotti, M.; Marliere, C., Stress-enhanced ion diffusion at the vicinity of a crack tip as evidenced by atomic force microscopy in silicate glasses. *J. Non-Cryst. Solids* **2007**, *353* (1), 51-68.
10. Bechgaard, T. K.; Mauro, J. C.; Smedskjaer, M. M., Time and humidity dependence of indentation cracking in aluminosilicate glasses. *J. Non-Cryst. Solids* **2018**, *491*, 64-70.
11. Surdyka, N. D.; Pantano, C. G.; Kim, S. H., Environmental effects on initiation and propagation of surface defects on silicate glasses: scratch and fracture toughness study. *Appl. Phys. A* **2014**, *116*, 519-528.
12. Lai, Y.; Gu, F.; Yu, J.; He, H., Environment dependence of hardness and fracture toughness of soda lime silica glass in humid and liquid conditions. *J. Non-Cryst. Solids* **2021**, *569*, 120985.
13. Waurischk, T.; Reinsch, S.; Rouxel, T.; Behrens, H.; Deubener, J.; Müller, R., Vacuum crack growth in alkali silicate glasses. *J. Non-Cryst. Solids* **2021**, *572*, 121094.
14. Wiederhorn, S.; Johnson, H.; Diness, A.; Heuer, A., Fracture of glass in vacuum. *J. Amer. Ceram. Soc.* **1974**, *57* (8), 336-341.
15. Grutzik, S.; Strong, K.; Rimsza, J., Kinetic model for prediction of subcritical crack growth, crack tip relaxation, and static fatigue threshold in silicate glass. *J. Non-Cryst. Solids: X* **2022**, *16*, 100134.
16. Markworth, A. J., Application of transition-rate theory to an atomistic model of environmentally assisted fracture. *Mater. Lett.* **1984**, *2* (4), 333-336.
17. Xu, Z.; Le, J.-L., On power-law tail distribution of strength statistics of brittle and quasibrittle structures. *Eng. Fract. Mech.* **2018**, *197*, 80-91.
18. Bažant, Z. P.; Le, J.-L.; Bazant, M. Z. In *Atomistic fracture and nano-macro transition for strength and lifetime statistics of quasibrittle structures*, 12th International Conference on Fracture 2009, ICF-12, 2009; pp 6559-6568.
19. Rimsza, J. M.; Jones, R. E.; Criscenti, L. J., Crack propagation in silica from reactive classical molecular dynamics simulations. *J. Amer. Ceram. Soc.* **2018**, *101* (4), 1488-1499.

20. Hou, D.; Zhu, Y.; Lu, Y.; Li, Z., Mechanical properties of calcium silicate hydrate (C–S–H) at nano-scale: A molecular dynamics study. *Mater. Chem. Phys.* **2014**, *146* (3), 503-511.
21. Chowdhury, S. C.; Haque, B. Z.; Gillespie, J. W., Molecular dynamics simulations of the structure and mechanical properties of silica glass using ReaxFF. *J. Mater. Sci.* **2016**, *51*, 10139-10159.
22. Chowdhury, S. C.; Wise, E. A.; Ganesh, R.; Gillespie Jr, J. W., Effects of surface crack on the mechanical properties of Silica: A molecular dynamics simulation study. *Eng. Fract. Mech.* **2019**, *207*, 99-108.
23. Mei, H.; Yang, Y.; van Duin, A. C.; Sinnott, S. B.; Mauro, J. C.; Liu, L.; Fu, Z., Effects of water on the mechanical properties of silica glass using molecular dynamics. *Acta Mater.* **2019**, *178*, 36-44.
24. Murray, S. J.; Subramani, V. J.; Selvam, R. P.; Hall, K. D., Molecular dynamics to understand the mechanical behavior of cement paste. *Transp. Res. Rec.* **2010**, *2142* (1), 75-82.
25. Murillo, J. S. R.; Bachlechner, M. E.; Campo, F. A.; Barbero, E. J., Structure and mechanical properties of silica aerogels and xerogels modeled by molecular dynamics simulation. *J. Non-Cryst. Solids* **2010**, *356* (25-27), 1325-1331.
26. Pedone, A.; Malavasi, G.; Menziani, M. C.; Segre, U.; Cormack, A. N., Molecular dynamics studies of stress– strain behavior of silica glass under a tensile load. *Chem. Mater.* **2008**, *20* (13), 4356-4366.
27. Hou, D.; Zhao, T.; Wang, P.; Li, Z.; Zhang, J., Molecular dynamics study on the mode I fracture of calcium silicate hydrate under tensile loading. *Eng. Fract. Mech.* **2014**, *131*, 557-569.
28. Muralidharan, K.; Oh, K.-D.; Deymier, P.; Runge, K.; Simmons, J., Molecular dynamics simulations of atomic-level brittle fracture mechanisms in amorphous silica. *J. Mater. Sci.* **2007**, *42*, 4159-4169.
29. Rimsza, J. M.; Jones, R. E.; Criscenti, L. J., Chemical effects on subcritical fracture in silica from molecular dynamics simulations. *J. Geophys. Res.: Solid Earth* **2018**, *123* (11), 9341-9354.
30. Rimsza, J. M.; Jones, R. E.; Criscenti, L. J., Mechanisms of silica fracture in aqueous electrolyte solutions. *Front. Mater.* **2019**, *6*, 79.
31. Rimsza, J. M.; Grutzik, S. J.; Jones, R. E., Inelastic relaxation in silica via reactive molecular dynamics. *J. Amer. Ceram. Soc.* **2022**, *105* (4), 2517-2526.
32. Hahn, S. H.; Rimsza, J.; Criscenti, L.; Sun, W.; Deng, L.; Du, J.; Liang, T.; Sinnott, S. B.; Van Duin, A. C., Development of a ReaxFF Reactive Force Field for NaSiO<sub>x</sub>/Water Systems and Its Application to Sodium and Proton Self-Diffusion. *J. Phys. Chem. C* **2018**, *122* (34), 19613-19624.
33. Rimsza, J. M.; Jones, R. E., Fracture mechanisms of sodium silicate glasses. *Int. J. Appl. Glass Sci.* **2023**, *14* (1), 27-37.
34. Chenoweth, K.; Van Duin, A. C.; Goddard, W. A., ReaxFF reactive force field for molecular dynamics simulations of hydrocarbon oxidation. *J. Phys. Chem. A* **2008**, *112* (5), 1040-1053.
35. Van Duin, A. C.; Dasgupta, S.; Lorant, F.; Goddard, W. A., ReaxFF: a reactive force field for hydrocarbons. *J. Phys. Chem. A* **2001**, *105* (41), 9396-9409.
36. He, B.; Vo, T.; Newell, P., Investigation of fracture in porous materials: a phase-field fracture study informed by ReaxFF. *Eng. Comput.* **2022**, *38* (6), 5617-5633.

37. Huang, R.; Sun, Y.; Yang, Z.; Liu, Y.; Yue, S., A novel ReaxFF multi-scale method for analyzing the fracture behavior of the CeO<sub>2</sub>. *Comput. Mater. Sci.* **2023**, *219*, 112002.
38. Rahman, M. H.; Chowdhury, E. H.; Hong, S., High temperature oxidation of monolayer MoS<sub>2</sub> and its effect on mechanical properties: A ReaxFF molecular dynamics study. *Surf. Interfaces.* **2021**, *26*, 101371.
39. Rimsza, J.; Ilgen, A., Water weakening of calcium oxide. *J. Phys. Chem. C* **2022**, *126* (22), 9493-9501.
40. Deng, L.; Urata, S.; Takimoto, Y.; Miyajima, T.; Hahn, S. H.; van Duin, A. C.; Du, J., Structural features of sodium silicate glasses from reactive force field-based molecular dynamics simulations. *J. Am. Ceram. Soc.* **2020**, *103* (3), 1600-1614.
41. Du, J.; Cormack, A. N., Molecular dynamics simulation of the structure and hydroxylation of silica glass surfaces. *J. Am. Ceram. Soc.* **2005**, *88* (9), 2532-2539.
42. Yu, Y.; Wang, B.; Wang, M.; Sant, G.; Bauchy, M., Revisiting silica with ReaxFF: Towards improved predictions of glass structure and properties via reactive molecular dynamics. *J. Non-Cryst. Solids* **2016**, *443*, 148-154.
43. Pedone, A.; Malavasi, G.; Menziani, M. C.; Cormack, A. N.; Segre, U., A new self-consistent empirical interatomic potential model for oxides, silicates, and silica-based glasses. *J. Phys. Chem. B* **2006**, *110* (24), 11780-11795.
44. Plimpton, S., Fast parallel algorithms for short-range molecular dynamics. *J. Comput. Phys.* **1995**, *117* (1), 1-19.
45. Zimmerman, J. A.; Jones, R. E., The application of an atomistic J-integral to a ductile crack. *J. Phys.: Condens. Matter* **2013**, *25* (15), 155402.
46. Lawn, B.; Wilshaw, R., Indentation fracture: principles and applications. *J. Mater. Sci.* **1975**, *10* (6), 1049-1081.
47. Hutchinson, J., Singular behaviour at the end of a tensile crack in a hardening material. *J. Mech. Phys. Solids* **1968**, *16* (1), 13-31.
48. Rountree, C.; Prades, S.; Bonamy, D.; Bouchaud, E.; Kalia, R.; Guillot, C., A unified study of crack propagation in amorphous silica: Using experiments and simulations. *J. Alloys Compd.* **2007**, *434*, 60-63.
49. Rountree, C. L.; Kalia, R. K.; Lidorikis, E.; Nakano, A.; Van Brutzel, L.; Vashishta, P., Atomistic aspects of crack propagation in brittle materials: Multimillion atom molecular dynamics simulations. *Annu. Rev. Mater. Res.* **2002**, *32* (1), 377-400.
50. Wilson, M. A.; Grutzik, S. J.; Chandross, M., Continuum stress intensity factors from atomistic fracture simulations. *CMAME* **2019**, *354*, 732-749.
51. Zhang, Z.; Ispas, S.; Kob, W., Fracture of silicate glasses: Microcavities and correlations between atomic-level properties. *Phys. Rev. Mater.* **2022**, *6* (8), 085601.
52. Yuan, X.; Cormack, A. N., Local structures of MD-modeled vitreous silica and sodium silicate glasses. *J. Non-Cryst. Solids* **2001**, *283* (1-3), 69-87.
53. Ren, M.; Deng, L.; Du, J., Surface structures of sodium borosilicate glasses from molecular dynamics simulations. *J. Amer. Ceram. Soc.* **2017**, *100* (6), 2516-2524.
54. Ren, M.; Deng, L.; Du, J., Bulk, surface structures and properties of sodium borosilicate and boroaluminosilicate nuclear waste glasses from molecular dynamics simulations. *J. Non-Cryst. Solids* **2017**, *476*, 87-94.
55. Cormack, A.; Du, J.; Zeitler, T., Sodium ion migration mechanisms in silicate glasses probed by molecular dynamics simulations. *J. Non-Crystalline Solids* **2003**, *323* (1-3), 147-154.

Supporting Information for:

## Inelastic Relaxation Processes in Amorphous Sodium Silicates

Jessica M. Rimsza<sup>1</sup> and Reese Jones<sup>2</sup>

<sup>1</sup>Geochemistry Department, Sandia National Laboratories, Albuquerque, NM USA

<sup>2</sup> Mechanics of Materials, Sandia National Laboratories, Livermore, CA USA

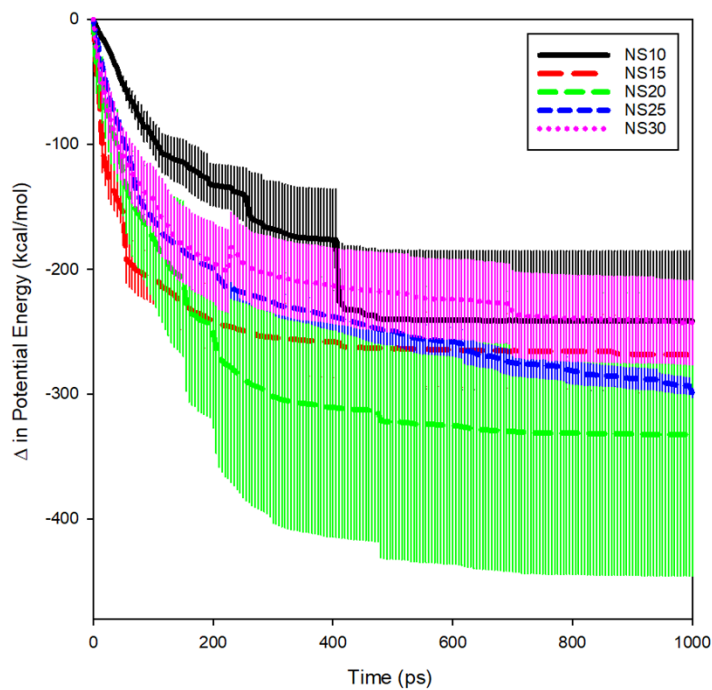


Figure S1: Change in potential energy of sodium silicate glass during 1000ps of inelastic relaxation.

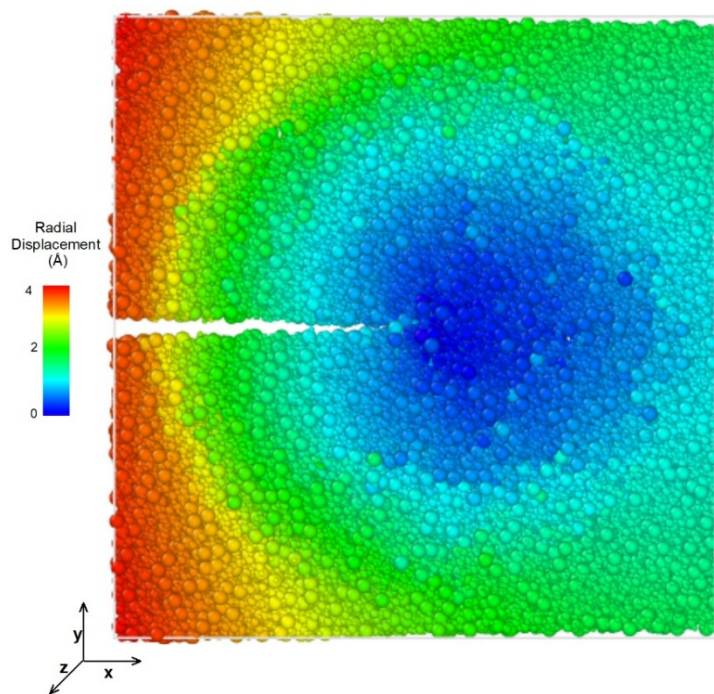


Figure S2: Radial displacement field prior to relaxation used to apply far-field loading.

Na/Si/O/H ReaxFF Forcefield

Reactive MD-force field: Na/Si/O/H force field 2018

39 ! Number of general parameters  
 50.0000 !Overcoordination parameter  
 9.5469 !Overcoordination parameter  
 1.6725 !Valency angle conjugation parameter  
 1.7224 !Triple bond stabilisation parameter  
 6.8702 !Triple bond stabilisation parameter  
 60.4850 !C2-correction  
 1.0588 !Undercoordination parameter  
 4.6000 !Triple bond stabilisation parameter  
 12.1176 !Undercoordination parameter  
 13.3056 !Undercoordination parameter  
 -40.0000 !Triple bond stabilization energy  
 0.0000 !Lower Taper-radius  
 10.0000 !Upper Taper-radius  
 2.8793 !Not used  
 33.8667 !Valency undercoordination  
 6.0891 !Valency angle/lone pair parameter  
 1.0563 !Valency angle  
 2.0384 !Valency angle parameter  
 6.1431 !Not used  
 6.9290 !Double bond/angle parameter  
 0.3989 !Double bond/angle parameter: overcoord  
 3.9954 !Double bond/angle parameter: overcoord  
 -2.4837 !Not used  
 5.7796 !Torsion/BO parameter  
 10.0000 !Torsion overcoordination  
 1.9487 !Torsion overcoordination  
 -1.2327 !Conjugation 0 (not used)  
 2.1645 !Conjugation  
 1.5591 !vdWaals shielding  
 0.1000 !Cutoff for bond order (\*100)  
 1.7602 !Valency angle conjugation parameter  
 0.6991 !Overcoordination parameter  
 50.0000 !Overcoordination parameter  
 1.8512 !Valency/lone pair parameter  
 0.5000 !Not used  
 20.0000 !Not used  
 5.0000 !Molecular energy (not used)  
 0.0000 !Molecular energy (not used)  
 0.7903 !Valency angle conjugation parameter

6 ! Nr of atoms; cov.r; valency;a.m;Rvdw;Evdw;gammaEEM;cov.r2;#  
 alfa;gammavdW;valency;Eunder;Eover;chiEEM;etaEEM;n.u.  
 cov r3;Elp;Heat inc.;n.u.;n.u.;n.u.;n.u.  
 ov/un;val1;n.u.;val3,vval4

C 1.3817 4.0000 12.0000 1.8903 0.1838 0.6544 1.1341 4.0000  
9.7559 2.1346 4.0000 34.9350 79.5548 5.4088 6.0000 0.0000  
1.2114 0.0000 202.2908 8.9539 34.9289 13.5366 0.8563 0.0000  
-2.8983 2.5000 1.0564 4.0000 2.9663 0.0000 0.0000 0.0000  
H 0.8930 1.0000 1.0080 1.3550 0.0930 0.8203 -0.1000 1.0000  
8.2230 33.2894 1.0000 0.0000 121.1250 3.7248 9.6093 1.0000  
-0.1000 0.0000 61.6606 3.0408 2.4197 0.0003 1.0698 0.0000  
-19.4571 4.2733 1.0338 1.0000 2.8793 1.0000 0.2000 12.0000  
O 1.2450 2.0000 15.9990 2.3890 0.1000 1.0898 1.0548 6.0000  
9.7300 13.8449 4.0000 37.5000 116.0768 8.5000 8.3122 2.0000  
0.9049 0.4056 59.0626 3.5027 0.7640 0.0021 0.9745 0.0000  
-3.5500 2.9000 1.0493 4.0000 2.9225 1.3000 0.2000 13.0000  
Si 2.1932 4.0000 28.0600 1.8951 0.1737 0.8112 1.2962 4.0000  
11.3429 5.2054 4.0000 21.7115 139.9309 4.0081 5.7104 0.0000  
-1.0000 0.0000 128.2031 9.0751 23.8188 0.8381 0.8563 0.0000  
-4.1684 2.0754 1.0338 4.0000 2.5791 1.4000 0.2000 13.0000  
Na 1.7878 1.0000 22.9898 2.6441 0.2588 0.8476 -1.0000 1.0000  
9.0003 2.5000 1.0000 0.0000 0.0000 -3.4731 8.1298 0.0000  
-1.0000 0.0000 23.0445 100.0000 1.0000 0.0000 0.8563 0.0000  
-4.1479 3.9900 1.0338 8.0000 2.5791 0.0000 0.0000 0.0000  
X -0.1000 2.0000 1.0080 2.0000 0.0000 1.0000 -0.1000 6.0000  
10.0000 2.5000 4.0000 0.0000 0.0000 8.5000 1.5000 0.0000  
-0.1000 0.0000 127.6226 8.7410 13.3640 0.6690 0.9745 0.0000  
-11.0000 2.7466 1.0338 6.2998 2.8793 0.0000 0.0000 0.0000  
14 ! Nr of bonds; Edis1;LPpen;n.u.;pbe1;pbo5;l3corr;pbo6  
pbe2;pbo3;pbo4;n.u.;pbo1;pbo2;ovcorr  
1 1 158.2004 99.1897 78.0000 -0.7738 -0.4550 1.0000 37.6117 0.4147  
0.4590 -0.1000 9.1628 1.0000 -0.0777 6.7268 1.0000 0.0000  
1 2 169.4760 0.0000 0.0000 -0.6083 0.0000 1.0000 6.0000 0.7652  
5.2290 1.0000 0.0000 1.0000 -0.0553 6.9316 0.0000 0.0000  
2 2 153.3934 0.0000 0.0000 -0.4600 0.0000 1.0000 6.0000 0.7300  
6.2500 1.0000 0.0000 1.0000 -0.0790 6.0552 0.0000 0.0000  
1 3 100.9167 136.3836 65.3877 0.3895 -0.3906 1.0000 18.8159 0.6674  
1.1202 -0.3411 9.1099 1.0000 -0.1966 5.6975 0.0000 0.0000  
3 3 142.2858 145.0000 50.8293 0.2506 -0.1000 1.0000 29.7503 0.6051  
0.3451 -0.1055 9.0000 1.0000 -0.1225 5.5000 1.0000 0.0000  
2 3 160.0000 0.0000 0.0000 -0.5725 0.0000 1.0000 6.0000 0.5626  
1.1150 1.0000 0.0000 0.0000 -0.0920 4.2790 0.0000 0.0000  
1 4 108.3910 95.0233 0.0000 0.1129 -0.5558 1.0000 17.2117 0.4568  
0.2424 -0.2378 10.1163 1.0000 -0.1020 5.7156 1.0000 0.0000  
2 4 250.0000 0.0000 0.0000 -0.7128 0.0000 1.0000 6.0000 0.1186  
18.5790 1.0000 0.0000 1.0000 -0.0731 7.4983 0.0000 0.0000  
3 4 261.9074 5.9533 0.0000 -0.6223 -0.3000 1.0000 36.0000 0.7275  
10.1541 -0.2366 29.7817 1.0000 -0.1083 8.5924 6.0658 0.0000  
4 4 70.9120 54.0531 30.0000 0.4931 -0.3000 1.0000 16.0000 0.0392  
0.2476 -0.8055 7.1248 1.0000 -0.1009 8.7229 0.0000 0.0000

```

2 5 26.7569 0.0000 0.0000 1.0000 -0.3000 1.0000 36.0000 0.0100
   0.5785 -0.3500 25.0000 1.0000 -0.2601 6.6137 1.0000 0.0000
3 5 28.0000 0.0000 0.0000 0.4351 -0.3000 1.0000 36.0000 0.0656
   18.6859 -0.3500 25.0000 1.0000 -0.1391 7.4280 1.0000 0.0000
4 5 0.1000 0.0000 0.0000 0.2500 -0.5000 1.0000 35.0000 0.6000
   0.5000 -0.5000 20.0000 1.0000 -0.2000 10.0000 1.0000 0.0000
5 5 72.6003 0.0000 0.0000 -0.7273 0.3000 0.0000 25.0000 0.1919
   6.6441 -0.4000 12.0000 1.0000 -0.0345 5.0063 0.0000 0.0000
9  ! Nr of off-diagonal terms; Ediss;Ro;gamma;rsigma;rpi;rpi2
1 2 0.1239 1.4004 9.8467 1.1210 -1.0000 -1.0000
2 3 0.0283 1.2885 10.9190 0.9215 -1.0000 -1.0000
1 3 0.0647 2.0109 10.0105 1.3177 1.2052 1.0682
1 4 0.0541 2.0811 13.5179 1.7778 1.5840 -1.0000
2 4 0.2000 1.5207 12.9535 1.2125 -1.0000 -1.0000
3 4 0.2000 1.9048 10.8374 1.7163 1.2444 -1.0000
2 5 0.1100 1.8410 9.1430 1.7735 -1.0000 -1.0000
3 5 0.1497 1.5719 13.3058 1.6111 -1.0000 -1.0000
4 5 0.1174 1.9434 17.1734 -1.0000 -1.0000 -1.0000
44 ! Nr of angles;at1;at2;at3;Thetao,o;ka;kb;pv1;pv2;val(bo)
1 1 1 59.0573 30.7029 0.7606 0.0000 0.7180 6.2933 1.1244
1 1 2 65.7758 14.5234 6.2481 0.0000 0.5665 0.0000 1.6255
2 1 2 70.2607 25.2202 3.7312 0.0000 0.0050 0.0000 2.7500
1 2 2 0.0000 0.0000 6.0000 0.0000 0.0000 0.0000 1.0400
1 2 1 0.0000 3.4110 7.7350 0.0000 0.0000 0.0000 1.0400
2 2 2 0.0000 27.9213 5.8635 0.0000 0.0000 0.0000 1.0400
1 1 3 53.9517 7.8968 2.6122 0.0000 3.0000 58.6562 1.0338
3 1 3 76.9627 44.2852 2.4177 -25.3063 1.6334 -50.0000 2.7392
2 1 3 65.0000 16.3141 5.2730 0.0000 0.4448 0.0000 1.4077
1 3 1 72.6199 42.5510 0.7205 0.0000 2.9294 0.0000 1.3096
1 3 3 81.9029 32.2258 1.7397 0.0000 0.9888 68.1072 1.7777
3 3 3 80.7324 30.4554 0.9953 0.0000 3.0000 50.0000 1.0783
1 3 2 70.1101 13.1217 4.4734 0.0000 0.8433 0.0000 3.0000
2 3 3 75.6935 50.0000 2.0000 0.0000 1.0000 0.0000 1.1680
2 3 2 85.8000 9.8453 2.2720 0.0000 2.8635 0.0000 1.5800
1 2 3 0.0000 25.0000 3.0000 0.0000 1.0000 0.0000 1.0400
3 2 3 0.0000 15.0000 2.8900 0.0000 0.0000 0.0000 2.8774
2 2 3 0.0000 8.5744 3.0000 0.0000 0.0000 0.0000 1.0421
4 4 4 78.5339 36.4328 1.0067 0.0000 0.1694 0.0000 1.6608
2 4 4 77.2616 5.0190 7.8944 0.0000 4.0000 0.0000 1.0400
2 4 2 75.7983 14.4132 2.8640 0.0000 4.0000 0.0000 1.0400
3 4 4 90.6812 31.1846 4.4543 0.0000 0.5073 0.0000 2.1809
2 4 3 73.6998 40.0000 1.8782 0.0000 4.0000 0.0000 1.1290
3 4 3 80.1361 36.2368 0.9504 0.0000 0.2624 0.0000 2.0787
4 3 4 80.4450 6.0739 1.7731 0.0000 3.2548 0.0000 1.0422
2 3 4 86.7611 7.1742 1.4013 0.0000 1.4999 0.0000 1.0400
3 3 4 103.4529 26.9589 1.3470 0.0000 1.7728 0.0000 1.3091

```

2	2	4	0.0000	47.1300	6.0000	0.0000	1.6371	0.0000	1.0400	
4	2	4	0.0000	27.4206	6.0000	0.0000	1.6371	0.0000	1.0400	
3	2	4	0.0000	5.0000	1.0000	0.0000	1.0000	0.0000	1.2500	
1	1	4	72.5239	22.3583	2.0393	0.0000	1.0031	0.0000	1.0400	
1	4	1	69.1709	18.9268	2.1226	0.0000	1.0031	0.0000	1.0400	
4	1	4	68.6453	18.7377	2.0496	0.0000	1.0031	0.0000	1.0400	
1	4	4	68.9902	19.7021	2.0587	0.0000	1.0031	0.0000	1.0400	
2	1	4	72.6403	13.6964	2.4702	0.0000	1.0000	0.0000	1.0400	
1	4	2	71.8708	14.6864	2.4702	0.0000	1.0000	0.0000	1.0400	
1	3	4	85.8521	12.6881	1.0112	0.0000	1.0000	0.0000	1.3220	
1	4	3	71.7524	35.8987	1.5000	0.0000	1.0000	0.0000	1.0487	
3	1	4	70.0000	5.0250	1.0000	0.0000	1.0000	0.0000	1.2500	
1	2	4	0.0000	2.5000	1.0000	0.0000	1.0000	0.0000	1.2500	
3	5	3	100.0000	45.9627	3.0941	0.0000	3.2848	0.0000	2.0000	
2	3	5	87.9313	7.1387	3.0639	0.0000	1.5000	0.0000	1.5554	
5	3	5	84.9984	6.4965	1.5553	0.0000	1.0368	0.0000	2.0000	
4	3	5	95.9867	2.0000	5.0000	0.0000	0.8452	0.0000	1.0000	
31	! Nr of torsions;at1;at2;at3;at4;;V1;V2;V3;V2(BO);vconj;n.u;n									
1	1	1	1	-0.2500	34.7453	0.0288	-6.3507	-1.6000	0.0000	0.0000
1	1	1	2	-0.2500	29.2131	0.2945	-4.9581	-2.1802	0.0000	0.0000
2	1	1	2	-0.2500	31.2081	0.4539	-4.8923	-2.2677	0.0000	0.0000
1	1	1	3	-0.5740	22.4215	0.8787	-2.7603	-1.1000	0.0000	0.0000
2	1	1	3	1.8164	18.8479	0.5134	-7.0513	-1.0978	0.0000	0.0000
3	1	1	3	-2.5000	56.1599	-1.0000	-4.3607	-0.8614	0.0000	0.0000
1	1	3	1	2.5000	14.6490	1.0000	-2.5209	-0.9000	0.0000	0.0000
1	1	3	3	-0.0002	20.1851	0.1601	-9.0000	-2.0000	0.0000	0.0000
1	3	3	1	0.0002	80.0000	-1.5000	-4.4848	-2.0000	0.0000	0.0000
3	1	3	3	-0.1583	20.0000	1.5000	-9.0000	-2.0000	0.0000	0.0000
1	1	3	2	-2.2946	11.6826	-1.0000	-2.5000	-0.9000	0.0000	0.0000
2	1	3	1	-1.0402	26.8401	0.6384	-2.5000	-0.9000	0.0000	0.0000
2	1	3	2	-1.0000	66.0304	0.7580	-5.4593	-1.1000	0.0000	0.0000
2	1	3	3	2.1531	45.9655	1.0000	-2.5000	-2.8274	0.0000	0.0000
3	1	3	1	0.6706	80.0000	-0.2443	-4.7181	-3.0437	0.0000	0.0000
3	1	3	2	-1.0000	91.6742	-0.5000	-3.9849	-3.0476	0.0000	0.0000
1	3	3	2	-2.5000	-0.5181	0.0268	-5.4085	-2.9498	0.0000	0.0000
2	3	3	2	-2.1995	-25.0000	-1.0000	-2.6000	-0.9921	0.0000	0.0000
1	3	3	3	2.4118	-24.8219	0.9706	-2.5004	-0.9972	0.0000	0.0000
2	3	3	3	-2.5000	43.1840	-0.6826	-6.6539	-1.2407	0.0000	0.0000
3	3	3	3	-2.5000	-25.0000	1.0000	-2.5000	-0.9000	0.0000	0.0000
0	1	2	0	0.0000	0.0000	0.0000	0.0000	0.0000	0.0000	0.0000
0	2	2	0	0.0000	0.0000	0.0000	0.0000	0.0000	0.0000	0.0000
0	2	3	0	0.0000	0.1000	0.0200	-2.5415	0.0000	0.0000	0.0000
0	1	1	0	0.0000	50.0000	0.3000	-4.0000	-2.0000	0.0000	0.0000
0	3	3	0	0.5511	25.4150	1.1330	-5.1903	-1.0000	0.0000	0.0000
2	4	4	2	0.0000	0.0000	0.0640	-2.4426	0.0000	0.0000	0.0000
2	4	4	4	0.0000	0.0000	0.1587	-2.4426	0.0000	0.0000	0.0000

```
0 2 4 0 0.0000 0.0000 0.1200 -2.4847 0.0000 0.0000 0.0000
3 1 1 4 -0.5740 22.4215 0.8787 -2.7603 -1.1000 0.0000 0.0000
1 1 4 3 -0.5740 22.4215 0.8787 -2.7603 -1.1000 0.0000 0.0000
1 ! Nr of hydrogen bonds;at1;at2;at3;Rhb;Dehb;vhb1
3 2 3 2.1200 -3.5800 1.4500 19.5000
```